Improving the Thermosphere Ionosphere in a Whole Atmosphere Model by Assimilating GOLD Disk Temperatures

F. I. Laskar[1], N. M. Pedatella[2], M. V. Codrescu[3], R. W. Eastes[1], W. E. McClintock[1],

[1]Laboratory for Atmospheric and Space Physics, University of Colorado, Boulder, CO, USA

[2]High Altitude Observatory, National Center for Atmospheric Research, Boulder, CO, USA

[3]Space Weather Prediction Center, NOAA, Boulder, CO, USA

Key Points:

- A new approach has been developed to assimilate GOLD T_{disk} in WACCMX which is validated using independent measurements.
- Analysis states of both the thermosphere and ionosphere show improved agreement with independent measurements.
- Results demonstrate a great potential of the GOLD T_{disk} data to improve thermosphere-ionosphere data assimilation.

Corresponding author: Fazlul I. Laskar, `Fazlul.Laskar@Lasp.colorado.edu`

Abstract

Global-scale Observations of Limb and Disk (GOLD) disk measurements of far ultraviolet molecular nitrogen band emissions are used to retrieve column integrated disk temperatures (T_{disk}), which are representative of the lower-and-middle thermosphere. The present work develops a new approach to assimilate the T_{disk} in the Whole Atmosphere Community Climate Model with thermosphere-ionosphere eXtension (WACCMX) using the Data Assimilation Research Testbed (DART) ensemble adjustment Kalman filter. Nine days of data, 1 to 9 November 2018, are assimilated. Analysis state variables such as thermospheric effective temperature (T_{eff}, airglow layer integrated temperature), ratio of atomic oxygen to molecular nitrogen column densities (O/N_2), and column electron content are compared with a control simulation that is only constrained up to ∼50 km. It is observed that assimilation of the GOLD T_{disk} improves the analysis states when compared with the control simulation. The analysis and model states, particularly, T_{eff}, O/N_2, and Electron Column Density (ECD) are compared with their measurement counterparts for a validation of the assimilation. T_{eff} and O/N_2 are compared with GOLD T_{disk} and O/N_2. While, the ECD is compared with ground based Total Electron Content (TEC) measurements from Global Navigational Satellite System (GNSS) receivers. Root Mean Square Error (RMSE) improvements in T_{eff} and O/N_2 are about 10.8% and 22.6%, respectively. The RMSE improvement in analyses ECD is about 10% compared to the control simulation.

Plain Language Summary

Understanding the temperature and density variability of the thermosphere-ionosphere system is very important for satellite drag calculations and satellite communication. The thermosphere-ionosphere system is influenced by waves from the lower atmosphere and solar and geomagnetic forcing from above. For the characterization of this coupled system, realistic whole atmosphere ionosphere parameters are of great interest. The GOLD satellite mission provides daytime thermospheric temperature observations with unprecedented local time and spatial coverage. Including them with the lower and middle atmospheric observations in a whole atmosphere data assimilation system, we find that they improve the state of the thermosphere-ionosphere. This shows the promise of the GOLD disk temperatures in improving thermosphere-ionosphere states and their potential use to improve space weather forecast capabilities.

1 Introduction

Improvements in the satellite drag forecasts and satellite communication depend on a better understanding of the thermosphere-ionosphere (TI) system variability. Earth's TI system is coupled to the lower atmosphere by wave-dynamical forcing and to the solar and geomagnetic forcing from above. The lower atmospheric forcing also varies with location and time. Thus, for a better understanding of this coupled system, a global four dimensional dataset with good temporal and spatial resolution is needed. Satellite measurements from low-Earth orbit can provide good spatial coverage, but they lack local time coverage, unless a constellation of satellites is used. Ground based observations on the other hand have good local time coverage, but they are not available globally due to the significant fraction of the Earth that is covered by ocean. Moreover, the currently available whole atmosphere ionosphere thermosphere observations have data gaps at different altitudes and geographic locations. However, the currently available observations and state-of-the-art whole atmosphere model simulations can be combined in a data assimilation framework. Data assimilation combines observations with model forecasts to produce analysis states that can better estimate the current state of the TI system.

With time the whole atmosphere ionosphere thermosphere models are improving, and number of observations from the TI system and lower atmosphere are increasing. Therefore, we are in a great stage to do a whole atmosphere data assimilation by combing the models and the observations. There is a long-history of lower atmosphere data assimilation (Rienecker et al., 2011; Gelaro et al., 2017; Hersbach et al., 2020), but the whole atmosphere system data assimilation is relatively new. There have been significant developments in the assimilation of thermosphere-ionosphere observations such as, neutral density (Ren & Lei, 2020; M. V. Codrescu et al., 2004; Matsuo et al., 2013; S. M. Codrescu et al., 2018; Sutton, 2018; Mehta et al., 2018), thermospheric temperature (Laskar, Pedatella, et al., 2021), thermospheric airglow radiance (Cantrall et al., 2019), and electron content (Bust et al., 2004; Lee et al., 2012; Datta-Barua et al., 2013; Matsuo et al., 2013; Lin et al., 2015; Aa et al., 2016; Chen et al., 2016; Bust & Immel, 2020; Pedatella et al., 2020; He et al., 2020; Kodikara et al., 2021; Song et al., 2021; Forsythe et al., 2021). While these results were promising and showed that the assimilation of TI observations improves the model states, most were limited to using upper atmosphere only models or used limited thermospheric datasets from low-earth-orbit satellites or ionospheric only measurements or observing system simulation experiments. Furthermore, a majority of

them have not combined lower, middle, and upper atmosphere data in the assimilation. Also, the spatial and temporal coverage of thermospheric data available earlier were limited.

Temperature is one of the basic parameters in whole atmosphere models. Neutral temperature retrieved from Global-scale Observations of Limb and Disk (GOLD) disk measurements have increased the number of thermospheric observation in the recent years, which enables scope for a better whole atmosphere data assimilation that can potentially improve the specification of the TI system. Laskar, Pedatella, et al. (2021) performed a set of Observing System Simulation Experiments (OSSEs) to evaluate the impact of assimilating GOLD disk temperature (T_{disk}) observations on thermospheric temperature and dynamics. They found that the OSSE that includes the GOLD T_{disk} improved the model temperature root mean square error (RMSE) and bias by 5% and 71% when compared with the forecast state, and the improvements are 20% and 94% when compared with lower atmosphere only assimilation. Laskar, Pedatella, et al. (2021) also found that the migrating diurnal tide (DW1) and local diurnal tide over Americas improve by about 8% and 17%, respectively, upon assimilation of GOLD disk temperature (T_{disk}) observations. In the current study we assimilate actual GOLD T_{disk} in a whole atmosphere data assimilation system and assess their impact on the thermosphere-ionosphere parameters by validating analysis states with their measurement counterparts.

2 Data, Models, and Methodology

The primary dataset used is the GOLD T_{disk}, which has been assimilated in the Whole Atmosphere Community Climate Model with thermosphere-ionosphere eXtension (WACCMX). In addition to T_{disk}, lower and middle atmosphere data have also been assimilated. For validation of the analysis states from the assimilation system, independent measurements of GOLD O/N_2 and Global Navigation Satellite System Total Electron Content (GNSS-TEC) are also used. Further details of these data and models are given below.

2.1 GOLD T_{disk}

GOLD observed the Earth's thermosphere in the far ultraviolet wavelengths for over 18.5 hours each day, from 0610 to 0040 Universal Time (UT) of the next day (Eastes et

al., 2019, 2020; McClintock et al., 2020; Laskar et al., 2020). The primary GOLD observations are emission intensities in the far ultraviolet (FUV) range of 134.5 to 166.5 nm. Data for one full disk scan are available at every 30 minutes from 6-23 UT (Eastes et al., 2019, 2020; Laskar, Eastes, et al., 2021). The current investigation uses level 2 T_{disk} data (version 3) that are retrieved from 2×2 binned level-1C data, which are available in the GOLD web-page, `https://gold.cs.ucf.edu/` as 'Level 2 - TDISK'. The retrieval algorithm is an improvement of the previously used methods for limb measurements (Aksnes et al., 2006; Krywonos et al., 2012).

The 2×2 binned data have a spatial resolution of 250-km×250-km near nadir and it gets slightly coarse at view angles higher than 45° from nadir. The GOLD daytime disk scans in N_2 Lyman-Birge-Hopfield (LBH) bands are used to retrieve T_{disk} data. Effective altitude and contribution function (CF) of the T_{disk} varies with solar zenith angle (SZA) and emission angle (EA). The SZA variation of the CF is well quantified (Laskar, Pedatella, et al., 2021) and thus is included in the present assimilation. However, the EA effects are not yet included in the assimilation. But, it has been observed that the EA does not impact the CF for EAs below 50°, so the T_{disk} data having EA>50° are not included in this assimilation and analysis. This limit also restricts the latitude and longitude coverage, as shown in Figure 1, to about ±50° in latitude and about -10°W to -90°W in longitude. Also, for high SZA observations the signal to noise ratio (SNR) is low, which for the current V3 T_{disk} introduces a bias. Thus, the low SNR observations having SZA>65° are not considered in the analysis and assimilation.

2.2 GOLD O/N_2

GOLD disk measurements of OI-135.6 nm emission and N_2-LBH bands in the ∼134-162 nm wavelength range are used to retrieve the ratio of atomic oxygen to molecular nitrogen column densities ($\Sigma O/\Sigma N_2$) (Correira et al., 2021). For simplicity we use the notation O/N_2 instead of $\Sigma O/\Sigma N_2$. The disk O/N_2 has the same spatial and temporal coverage as T_{disk}. O/N_2 data are used here only for the comparison and validation of the analyses O/N_2. We use the 2×2 binned version 3 O/N_2 data, named as 'Level 2 - ON2' in the GOLD data repository. Also, as the GOLD O/N_2 is not optimized for auroral latitudes (Correira et al., 2021), the latitudes above ±60° are not used in the current analysis. Typical random, systematic, and model uncertainties in the GOLD O/N_2

142 are about 5%, 5%, and 30% to 40%, respectively. Note that the model uncertainty is a

143 bias with an unknown sign (Correira et al., 2021).

2.3 GNSS-TEC

145 The GNSS-TEC data used in this study are obtained from the madrigal database

146 (`https://cedar.openmadrigal.org`). Madrigal TEC maps are derived from worldwide

147 GNSS ground-based receivers. The vertical TEC data are available at 5 min temporal

148 and 1° by 1° spatial bins. Details on the TEC retrieval algorithm can be found in Rideout

149 and Coster (2006) and Vierinen et al. (2016). In the current study the TEC maps are

150 averaged over 20 minutes centered at every UT hour to compare them with the analy-

151 sis ECD from assimilation. The 20 minutes averaging is chosen to get enough satellite

152 passes over a particular spatial grid.

2.4 WACCMX

154 The WACCMX version 2.1 is a whole atmosphere general circulation model extend-

155 ing from the surface to the upper thermosphere (∼500-700 km depending on solar ac-

156 tivity) (Liu et al., 2018). WACCMX includes the chemical, dynamical, and physical pro-

157 cesses that are necessary to model the lower, middle, and upper atmospheres. The ther-

158 mosphere and ionosphere processes in WACCMX are similar to those in the NCAR Thermosphere-

159 Ionosphere-Electrodynamics General Circulation Model (TIE-GCM), including the trans-

160 port of O^+ and self-consistent electrodynamics as well as realistic solar and geomagnetic

161 forcing. The model horizontal resolution is $1.9° \times 2.5°$ in latitude and longitude, and the

162 vertical resolution is 0.25 scale height above ∼50 km.

2.5 SD-WACCMX

164 In this simulation the WACCMX horizontal winds and temperature are relaxed to-

165 wards Modern-Era Retrospective analysis for Research and Applications, Version 2 (MERRA2)

166 (Gelaro et al., 2017; Rienecker et al., 2011), so we name it as Specified Dynamics WAC-

167 CMX (SD-WACCMX). The relaxation or nudging to MERRA2 is up to 50 km altitude,

168 and the model is free-running above this altitude (Marsh, 2011). The SD-WACCMX is

169 used in this study as a control simulation. In addition to MERRA2, SD-WACCMX sim-

170 ulations (often referred here as SD) also use operational solar F10.7 cm flux and geomag-

171   netic Kp index for forcing and thus they can be used as a control simulation for the as-

172   sessment of the data assimilation states.
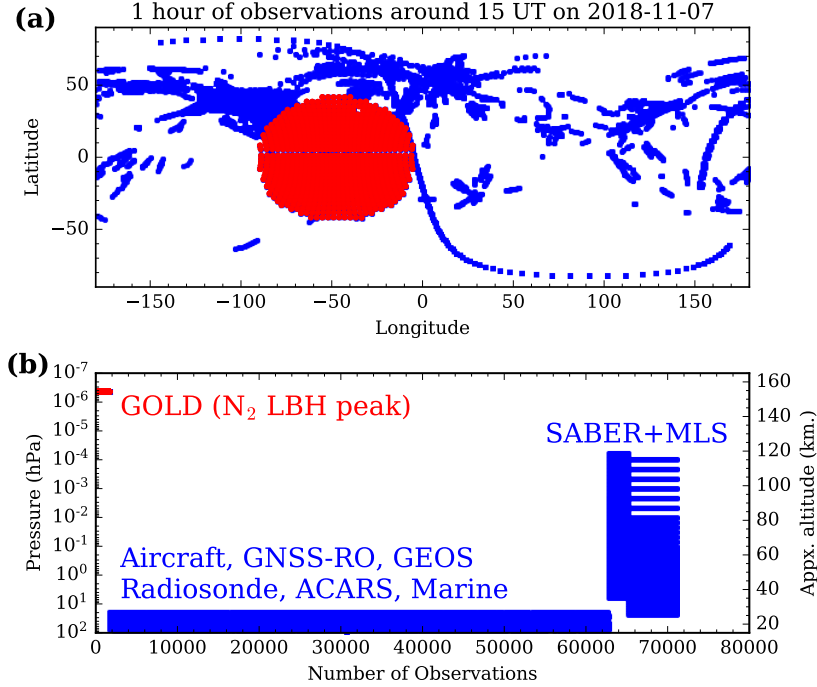
(a)

Figure 1.   Geo-locations (a), altitude or pressure and number of observations (b) that are as-
similated successfully during a representative hour on a particular day are shown. The red points
show the GOLD observations and blue points are the rest of the observations, which we term as
lower atmosphere observations including SABER and MLS.

2.6 WACCMX+DART

173

174   The data assimilation capability in WACCMX was initially implemented by Pedatella

175   et al. (2018) using DART (J. Anderson et al., 2009), which uses the ensemble adjustment

176   Kalman filter (J. L. Anderson, 2001). In the present work we assimilate lower and mid-

177   dle atmosphere as well as thermosphere observations in the WACCMX+DART. The lower

178   atmosphere measurements include conventional meteorological observations (i.e., tem-

179   peratures and winds from aircraft, radiosonde measurements, etc.), as well as GNSS ra-

180   dio occultation refractivity. Assimilation of these observations improves specifications

181   of the troposphere-stratosphere globally, which is important for the studies of the ver-

tical coupling of waves from lower-atmosphere to the thermosphere (Wang et al., 2011; Pedatella et al., 2014; McCormack et al., 2017; Pedatella et al., 2018).

In addition to lower altitude observations, middle atmosphere temperatures from Sounding of the Atmosphere using Broadband Emission Radiometry (SABER) instrument on the Thermosphere Ionosphere Mesosphere Energetics and Dynamics (TIMED) satellite and Aura Microwave Limb Sounder (Aura-MLS) are also used. Altitude coverage of temperature profiles extends from stratosphere to mesosphere-lower-thermosphere (MLT) altitudes (∼15-105 km for TIMED-SABER and ∼15-90 km for Aura-MLS). The latitude coverage of TIMED-SABER retrieved temperature alternates between 83°S-52°N (south viewing mode) and 83°N-52°S (north-viewing mode) (Remsberg et al., 2008). We performed 9 days (1 to 9 November 2018) of data assimilation, during which TIMED-SABER was in the north-viewing mode on 1 November only. From 2 to 9 November it was in the south viewing mode. While for the Aura-MLS it varies from 82°S-82°N (Schwartz et al., 2008). Though Aura-MLS and TIMED-SABER temperatures are middle atmospheric observations, for simplicity we refer to them here as part of lower atmosphere observations. Assimilation of these data has previously been demonstrated to improve specification of the MLT state and dynamics (Pedatella et al., 2014; McCormack et al., 2017; Laskar et al., 2019).

In addition to lower atmosphere observations, GOLD T_{disk} are used in the whole atmosphere assimilation. As the thermospheric dynamics can quickly change in response to changes in forcing conditions, we use a 1 hour assimilation frequency. Additionally, Pedatella et al. (2020) have shown that using a 1 hr data assimilation cycle and removal of second-order divergence damping in WACCMX+DART significantly improves tidal amplitudes, which were previously found to be too small (Pedatella et al., 2018). As full disk images are available at 30 minutes intervals during sunlit hours, a 1 hour interval will have sufficient data in the thermosphere. Also, the lower atmosphere analysis states in WACCMX+DART agree well with other lower atmospheric assimilations, for example, MERRA2 (McCormack et al., 2021).

Figure 1 shows the locations (in a) and altitude or pressure vs. number of observations (in b) that are assimilated successfully during a representative hour on a particular day. The red points show the GOLD observations and blue points are the rest of the observations, which we term as lower atmosphere observations, including TIMED-

Experiment	Observations Assimilated	Nudging Used	Model States Updated
SD (SD-WACCMX, Control Expt.)	N/A	MERRA2 U, V, T up to 50 km	N/A
DA1 (WAC-CMX +DART Expt. 1)	Meteorological, Aura-MLS-T, SABER-T, GOLD-T_{disk}	N/A	T
DA2 (WAC-CMX +DART Expt. 2)	Same as DA1	N/A	T, O, O_2, O^+

Table 1.   WACCMX simulation and data assimilation experiments used in this study are listed. U, V, T, N/A, SD, and DA stands for zonal wind, meridional wind, temperature, Not Applicable, Specified Dynamics, and Data Assimilation, respectively. Also, O, O_2, and O^+ refers to the mass mixing ratio of atomic oxygen, molecular oxygen, oxygen ion, respectively. The short forms of the experiments are presented in bold.

SABER and Aura-MLS. Note that the peak altitude of the N_2-LBH emission is shown here as a representative altitude of about 150 km, but in the assimilation the impact of T_{disk} is distributed over altitudes based on the SZA dependent CF (Laskar, Pedatella, et al., 2021). One can see that about 70000 observations per hour are assimilated. On average about 1.5 million observations per day are assimilated. The simulations used in this study are listed in Table 1. The SD-WACCMX is used in this study as the control simulation.

We have performed two WACCMX+DART assimilations. One that assimilates lower atmosphere and GOLD T_{disk} observations, but the direct impact of T_{disk} has been restricted only to the model temperature, referred to as DA1 in Table 1. The second experiment assimilates the same observations as the first experiment, but the T_{disk} observations directly impact the model T, O, O_2, and O^+, referred to as DA2 in Table 1. We used 40 ensemble members in the assimilation. In order to achieve sufficient spread in the ensemble members, we used Gaussian distributions of solar and geomagnetic forc-

228 ing parameters with mean as the actual value and standard deviations of 15 sfu for F10.7

229 cm flux and 1 for Kp index (i.e., $d_{F10.7} \sim \mathcal{N}(F10.7, 15^2)$ and $d_{K_p} \sim \mathcal{N}(K_p, 1^2)$). We

230 reset any F10.7 value less than 60 sfu to 60 sfu and any negative Kp to 0. The forcing

231 perturbation for each ensemble member remains the same for all the days. To avoid ar-

232 tifacts arising from initial ensemble members, the spinup duration for the two assimi-

233 lation runs are about 2 weeks i.e., each assimilation run starts from 15th October 2018.

3 Results

235 In order to assess and validate the performance of the assimilation we compare the

236 ensemble averaged analysis states to their measurement counterparts. For example, ef-

237 fective temperature (T_{eff}) from model simulation is compared with GOLD T_{disk}; O/N_2

238 is compared with GOLD O/N_2; and Electron Column Density (ECD) is compared with

239 the GNSS-TEC. Note that T_{eff} here refers to the vertically integrated GOLD equiva-

240 lent temperature that is calculated by integrating the model temperature profile weighted

241 by the SZA dependent CFs. Also, the ECD is similar to TEC, but the column integra-

242 tion is only to the topmost layer of WACCMX, which is about 480 km for the current

243 cases. Figure 2 shows a comparison of the local time and latitude variation of the GOLD

244 T_{disk} with T_{eff} from ensemble averaged states of the DA1 (DA1 T_{eff}) and SD-WACCMX

245 (SD T_{eff}) for 2 different days. The latitudes and local times are restricted to only those

246 locations and times where GOLD T_{disk} is being assimilated. Beyond those local time

247 and latitudes GOLD data are available, but we are not using them in the assimilation

248 as explained in Sections 2.1 and 2.2. Note that in this figure only a representative lon-

249 gitude of 48°W is shown, which is close to the sub-satellite point of GOLD.

250 It can be noted from Figure 2 that the broad variations between T_{disk} and DA1

251 T_{eff} are similar on both the days. On 5th November 2018 there was a moderate geo-

252 magnetic storm for which the average temperature is more than 100 K higher than 3rd

253 November 2018. Moreover, the morning temperatures are relatively warmer, particularly

254 between 40° and 50°S. These variations of the GOLD T_{disk} during geomagnetic events

255 have been reported and discussed in Laskar, Eastes, et al. (2021). These results suggest

256 that the data assimilation is driving the model temperature in the right direction i.e.,

257 closer to those observed. A quantitative estimate of the differences between them are given

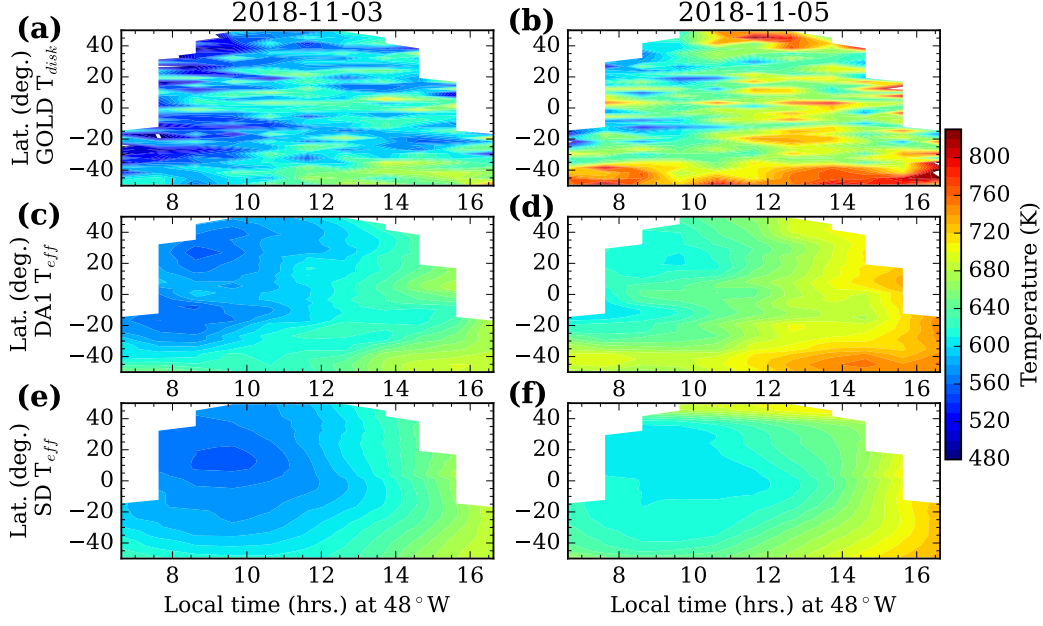258 later. Note that since both the assimilation experiments updated temperature directly

Figure 2. Local time and latitude variation of the GOLD T_{disk} compared with T_{eff} from DA1 (DA1 T_{eff}) and SD-WACCMX (SD T_{eff}).

at every assimilation step, the T_{eff} are almost the same for both DA cases. So, the T_{eff} for only the DA1 is shown here.

A change in temperature also impacts other states by altering the model dynamics. Therefore, assimilation of T_{disk} can also impact the O/N_2 ratio, which is another primary dataset from the GOLD mission. Figure 3 shows a comparison of GOLD O/N_2 with the O/N_2 from data assimilation and control simulation experiments, for the same 2 days shown in Figure 2. Note that the model O/N_2 values are calculated by integrating the O and N_2 profiles down to the altitude corresponding to $1.5 \times 10^{21} \mathrm{m}^{-2}$ of N_2, instead of $10^{21} \mathrm{m}^{-2}$ as suggested by Strickland et al. (1995). The resulting O/N_2 values closely correspond to those from GOLD. Unlike Figure 2, here the latitude range is extended to 60°N/S, as the GOLD O/N_2 are valid for those latitudes. We compare O/N_2 from the DA1 (c and d), DA2 (e and f), and SD (g and h) with the GOLD O/N_2 (a and b). Note that the GOLD O/N_2 observations have not been assimilated in any of the experiments. In the DA2 the GOLD T_{disk} observations also directly update the O, O_2, and O^+ mass mixing ratios in addition to temperature. The direct updating of these quantities impacts the neutral composition and ionosphere at every assimilation step and thus
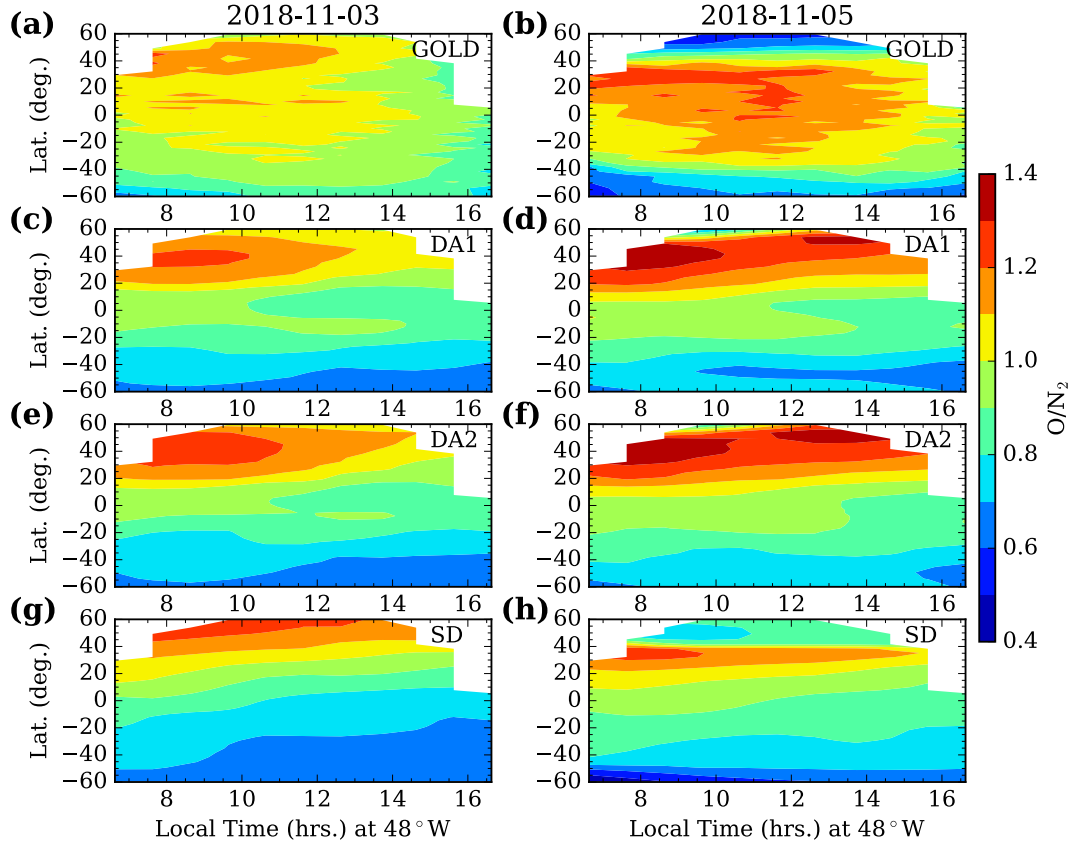
Figure 3. Same as Figure 2 but for the column integrated O/N$_2$ ratio. In addition to the DA1 the DA2 O/N$_2$ is also shown in (e and f).

275 they are expected to compare better than the indirectly updated states. It can be ob-

276 served from Figure 3 that the broad variations in O/N_2 agree well between GOLD O/N_2

277 and the two assimilation experiments. Though interhemispheric features in SD, the as-

278 similation experiments, and the observations match well, there are clear differences in

279 magnitudes and large-scale structures between them. For the quiet-day of 3rd Novem-

280 ber the two assimilation experiments show better agreement with GOLD O/N_2 compared

281 to the SD O/N_2. The highest discrepancy in O/N_2 can be seen on the storm day (right

282 panel) where the Northern higher-latitude depletion in the GOLD O/N_2 occurs relatively

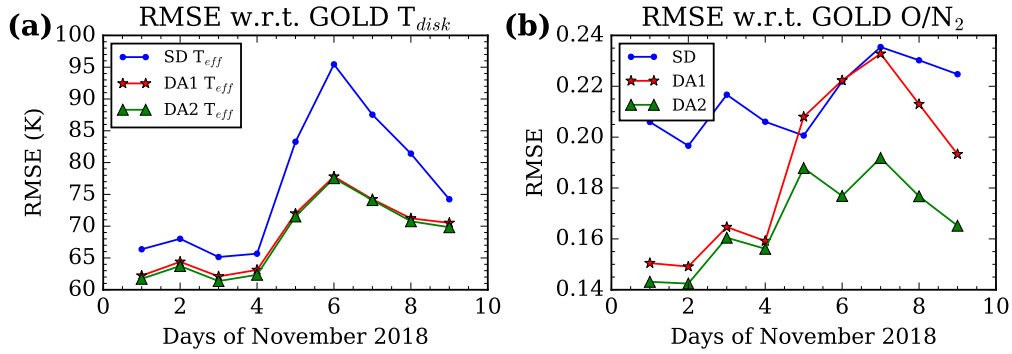283 at higher latitudes in DA1 and DA2 and is weaker in the SD.

Figure 4. The RMSEs in DA1 T_{eff} and DA2 T_{eff} with respect to GOLD T_{disk} are shown in (a) and similar RMSEs in O/N_2 are shown in (b). Note that the temperature RMSEs in the two DA runs, are clearly smaller than the SD. Also, the average O/N_2 RMSEs are better for the two assimilation runs compared to the SD, and DA2 has the best RMSE.

284 For a quantitative estimation of the above observed differences between actual mea-

285 surements and their data assimilation equivalents we calculate the Root Mean Square

286 Error (RMSE). The RMSE in SD T_{eff}, DA1 T_{eff}, and DA2 T_{eff} with respect to GOLD

287 T_{disk} are shown in Figure 4(a) for all 9 days. The RMSE for each day is calculated over

288 the whole disk and local time range as shown in Figure 2 for temperature and Figure

289 3 for O/N_2. Note that the temperature RMSEs in the two data assimilation runs are clearly

290 smaller than the SD. Also, the temperature RMSE for the two assimilation runs are al-

291 most the same, which is expected as both the assimilations updated model temperature

292 directly. The RMSEs in O/N_2 are shown in Figure 4(b). The average O/N_2 RMSEs are

293 better for the two assimilation runs compared with the SD, and DA2 has the best RMSE.

294   The pre-storm RMSEs are smaller compared with storm onset and recovery phase. Av-

295 erage RMSE improvements in effective temperature and O/N_2 compared to the SD are

296 about 10.8% and 22.6%, respectively. The improvements of pre-storm RMSE in T_{disk}

297 and O/N_2 are about 6.4% and 27.9% while during the storm they were about 15.5% and

298 17.4%, respectively. These results suggest that even though the storm times RMSEs are

299 larger, the percentage improvements are larger too.

300   For a more robust diagnosis of the relationship between SD T_{eff}, DA1 T_{eff}, and

301 DA2 T_{eff} with respect to GOLD T_{disk} for all the available latitudes and longitudes in

302 the disk scans between 10 to 20 UT during 1 to 9 November 2018 we make scatter di-

303 agrams as shown in Figure 5, where the red color represents high density points. Red

304 (solid) and blue (dashed) lines represent least square fitted straight line and one-to-one

305 (45° slope or gradient equal to one line) relationship. Correlation coefficients and fitted

306 linear equations are also given. From these scatter plots it can be seen that the major-

307 ity of the T_{disk} vs. DA2 T_{eff} points (in a) fall on the one-to-one line. But, for the T_{disk}

308 vs. SD T_{eff} (in e) comparison, the highest density observations (red points) deviate away

309 from the one-to-one linear relationship. Also, the correlation coefficient and gradient of

310 the fitted lines are better for the assimilation runs. Note that here also, only those ob-

311 servations are shown that fall within the 50° EA and 65° SZA limits. As the GOLD T_{disk}

312 has higher spread compared to DA2 T_{eff}, DA1 T_{eff}, and SD T_{eff} the shape of the scat-

313 ter plot is elongated towards the T_{disk} axis (in a, c, and e). Similar to temperature, the

314 O/N_2 scatter diagrams are shown in Figure 5(b, d, and f) but the EA and SZA restric-

315 tions are not applied here. The correlation coefficients for O/N_2 are small, though they

316 are statistically significant as p-values (probability that the correlation arises from noise)

317 are zero, suggesting a weak linear relationship. As the high density (red) points are mostly

318 located around a circle for the two assimilation cases, the linear correlation would not

319 be a great measure of the relationship between them. Therefore, we calculated the RMSE

320 for the two assimilations and SD with respect to GOLD O/N2. The RMSEs for the DA1,

321 DA2, and SD with respect to GOLD are 0.20, 0.17, and 0.23, respectively, suggesting that

322 the two DA runs perform better compared to SD. The distribution of points in the GOLD

323 T_{disk} vs. DA1 T_{eff} and GOLD T_{disk} vs. DA2 T_{eff} is nearly identical because the tem-

324 perature was updated directly in both the assimilations. However, the distributions in

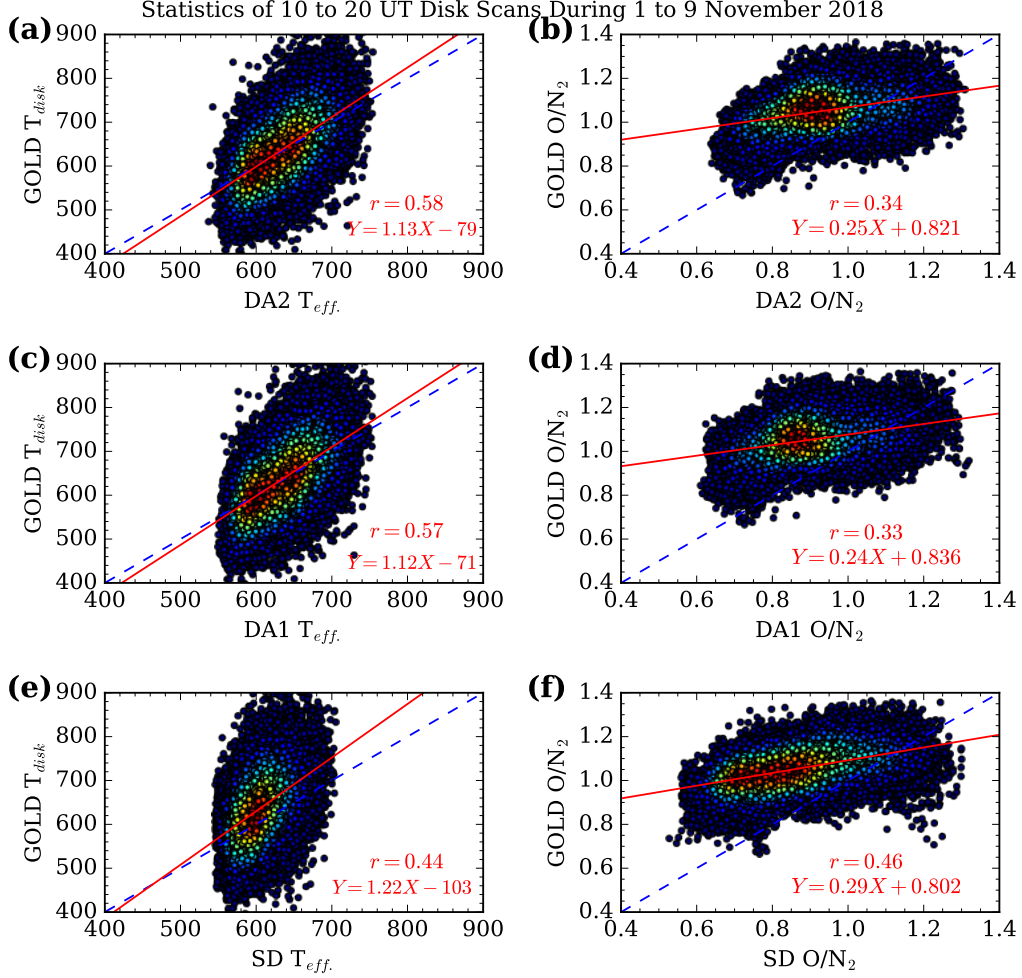325 O/N_2 in Figure 5(b and d) are significantly different.

Statistics of 10 to 20 UT Disk Scans During 1 to 9 November 2018

(a)

GOLD T_{disk} vs DA2 $T_{eff.}$

$r = 0.58$
$Y = 1.13X - 79$

(b)

GOLD O/N_2 vs DA2 O/N_2

$r = 0.34$
$Y = 0.25X + 0.821$

(c)

GOLD T_{disk} vs DA1 $T_{eff.}$

$r = 0.57$
$Y = 1.12X - 71$

(d)

GOLD O/N_2 vs DA1 O/N_2

$r = 0.33$
$Y = 0.24X + 0.836$

(e)

GOLD T_{disk} vs SD $T_{eff.}$

$r = 0.44$
$Y = 1.22X - 103$

(f)

GOLD O/N_2 vs SD O/N_2

$r = 0.46$
$Y = 0.29X + 0.802$

Figure 5. Scatter diagram of the GOLD T_{disk} and O/N_2 compared to their DA2, DA1, and SD equivalents are shown. For this analysis all the disk scans between 10 to 20 UT during 1 to 9 Nov. 2018 are used. The red regions in the scatter diagram represents highest density points. For the GOLD vs. DA2 the highest density points distribute around the one-to-one line (dashed), particularly for the temperature. The comparison w.r.t. SD for both temperature and O/N_2, on the other hand, is not as good.

Figure 6. Latitude and day-to-day variability of SD ECD (a), DA1 ECD (b), DA2 ECD (c), and GNSS-TEC (d) averaged over 55°W to 65°W longitude.

The 23% improvement in DA2 O/N$_2$, as seen in Figure 4, motivated us to analyze the electron content derived from the assimilations and compare them with independent TEC measurements. Figure 6 shows a latitude vs. day-to-day variation of ECD in SD (a), DA1 (b), DA2 (c), and GNSS-TEC (d) centered at around 60°W ($\pm5°$) longitude. This spatial bin has been chosen due to the greater availability of GNSS data in this region. As mentioned in section 2.3, the GNSS-TEC data are averaged over 20 minutes duration centered at every hour. Note that even with the 20 minute averaging, there are missing data, specifically between 20° and 40°N. This figure shows that the magnitudes of electron densities and some of the shape and temporal variabilities of Equatorial Ion-

335   ization Anomaly (EIA) in DA2 has better agreement with GNSS-TEC compared to the

336   DA1 and SD. Particularly, the northern mid-latitude enhanced DA2 ECDs are in bet-

337   ter agreement with GNSS-TEC. A quantification of the improvements is given at the end

338   of this section. Though there are improvements in DA2, the EIA latitude extent and hemi-

339   spheric asymmetries are not yet well reproduced in the assimilations. This could be due

340   to the fact that the temperature variability cannot fully reflect the changes in the iono-

341   sphere as the ionosphere is also influenced by E-region winds in addition to neutral and

342   ionospheric composition changes. We expect to have better agreement in the future when

343   the GOLD O/N$_2$ and other ionospheric dataset are assimilated in addition to the T$_{disk}$.

344   For a qualitative assessment of the improvements seen in the ionospheric electron

345   content, a comparison between SD-ECD (green), DA1 ECD (cyan), DA2 ECD (red), and

346   GNSS-TEC (blue) for a limited spatial region is shown in Figure 7(a). The RMSE (in

347   Figure 7b) and bias (in Figure 7c) with respect to GNSS-TEC are also shown. Except

348   for November 1st and 2nd and the night hours of each day (shaded regions, when GOLD

349   data are not assimilated), the other days' DA2 ECD has better agreement with GNSS-

350   TEC as can be inferred from the smaller values of the RMSE and bias. Some of the lo-

351   cal time variabilities also have better agreement with DA2. For example, the two-peak

352   structures in daytime GNSS-TEC on days 3 and 5 are better reproduced in the DA2 ECD,

353   while that on 8th has not been reproduced. The two peak structure is particularly strong

354   on November 3rd as indicated by downward arrows. Note the dates are in local time at

355   60°W. Also, the broader shape of the local time variability in GNSS-TEC match bet-

356   ter with DA2 ECD as can be seen on most days in Figure 7(a). Except for November

357   1st and 2nd, the night sector (shaded regions) has higher RMSEs, in general during the

358   last 4 hours of each day and particularly at the end of November 6th. This is expected

359   because the GOLD temperature are assimilated only during daylight sector and there-

360   fore they are not able to constrain the night-time dynamics. Including ionospheric and

361   O/N$_2$ observations in the assimilation would improve the results. The purpose of this

362   comparison is to demonstrate that the ionosphere is also improved upon assimilation of

363   GOLD T$_{disk}$, though there are still large RMSEs and biases. Quantitative estimates of

364   the differences, that vary with latitude and time, are given in Figure 8 and its discus-

365   sion as given below.

366   In Figure 3 we show that the GOLD O/N$_2$ has latitudinal differences from the DA

367   O/N$_2$. Also, we have seen in Figure 6 that the agreement between DA2 ECD and GNSS-
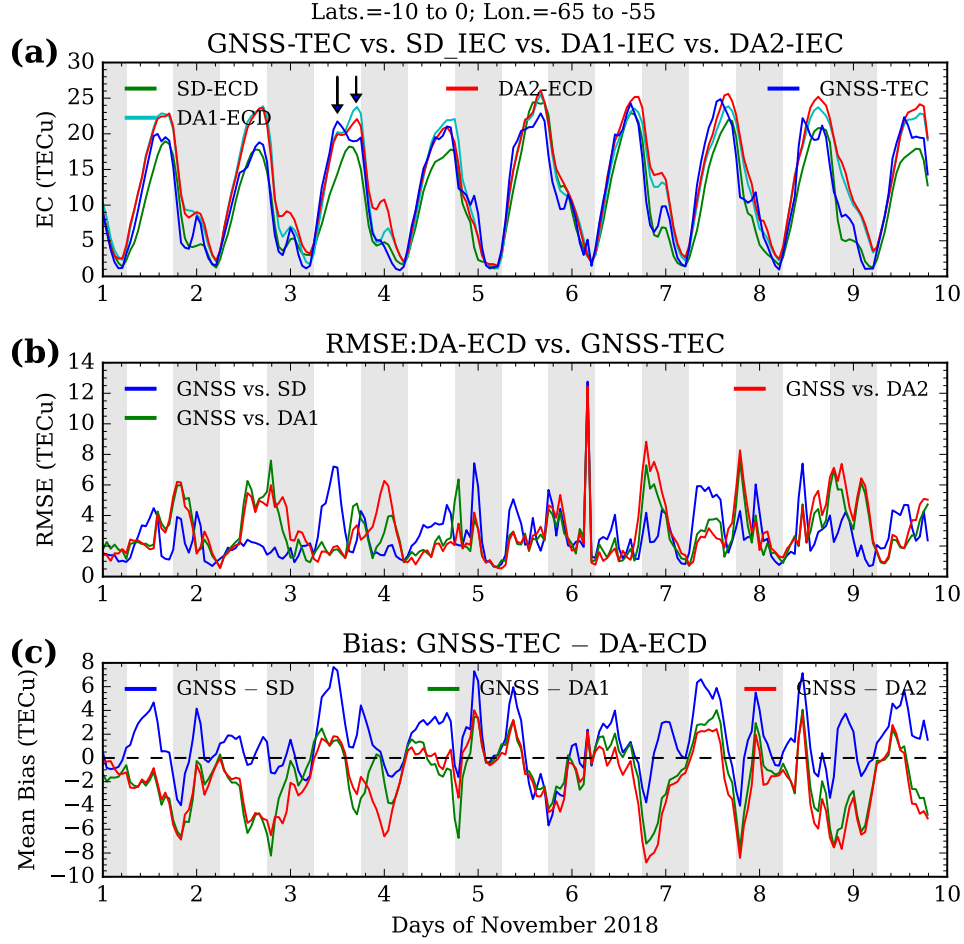
Figure 7. (a) Comparison of the SD ECD (green), DA1 ECD (cyan), DA2 ECD (red), and GNSS-TEC (blue) which are averaged over 10°S to 0°N and 55°W to 65°W. (b) RMSEs in GNSS-TEC vs. SD ECD (blue), GNSS-TEC vs. DA1 ECD (green), and GNSS-TEC vs. DA2 ECD (red). (c) Mean bias in GNSS-TEC vs. SD ECD (blue), GNSS-TEC vs. DA1 ECD (green), and GNSS-TEC vs. DA2 ECD (red) are shown. Two dashed arrows in (a) indicate example two-peak structure. The shaded regions represent nighttime, when GOLD data are not assimilated.

368 TEC varies with latitude. To investigate these latitudinal differences in TEC we have

369 calculated the RMSE and mean bias at every 10 degree latitude bin during the 9 days.

370 The RMSE and mean bias in electron contents from SD, DA1, and DA2 with respect

371 to GNSS TEC are shown in Figure 8. One can note that the lowest values of the RMSE

372 and bias are observed for the DA2, the red lines marked with stars. The RMSE and bias

373 at every latitude bin is calculated from all the $24 \times 9 = 216$ hours of data. The percent-

374 age improvements in RMSE for DA1 ECD and DA2 ECD with respect to GNSS-TEC

375 are about 3% and 10%, respectively. The 9 day average mean biases with respect to GNSS-

376 TEC for the SD, DA1, and DA2 are about 1.9, 0.5, and 0.2 TECu, respectively. Also,

377 the latitudinal average of absolute-biases are 1.92, 1.37, and 1.44 for SD, DA1, and DA2,

378 respectively. Though the latitudinal average of the mean biases is slightly smaller for the

379 DA2 compared to DA1, it is clear, from the absolute values, that the biases are smaller

380 for both the assimilations compared to SD. Also, the the mean bias is positive at higher

381 latitudes ($> 30°$) as seen in Figure 8(b). Since O/N_2 and TEC vary in proportion, to

382 a large extent, the smaller O/N_2 (from GOLD as shown in Figure 3b at the higher lat-

383 itudes compared to SD and DA) may produce the positive mean biases in TEC. Neg-

384 ative bias and high RMSE between 0 and 20°S for the DA2 also imply that the equa-

385 torial elctrodynamics, which is controlled by ionospheric E-region winds and composi-

386 tion, are not well constrained in the assimilations. Also, the night-time (when GOLD

387 data are not assimilated) electrodynamics, particularly pre-reversal enhancement that

388 is highly variable, contributes to poorer low-latitude results. But, overall these results

389 further emphasize that the DA2 – where in addition to temperature the O, O^+, and O_2

390 mixing ratios are updated directly – has the most improved thermosphere and ionosphere.

391 Overall, it can be observed that the RMSEs are lower in the Northern hemisphere com-

392 pared to the Southern hemisphere, which suggests that the Northern hemispheric vari-

393 abilities are better reproduced in the assimilation.

4 Conclusions

395 An investigation of the impact of GOLD T_{disk} assimilation on thermosphere-ionosphere

396 states is carried out using WACCMX+DART analysis states, GOLD measurements, and

397 GNSS-TEC. The salient results of this investigation are:

398 1. GOLD T_{disk} assimilation analysis states of the thermosphere-ionosphere show bet-

399 ter agreement with independent measurements than the control simulation.
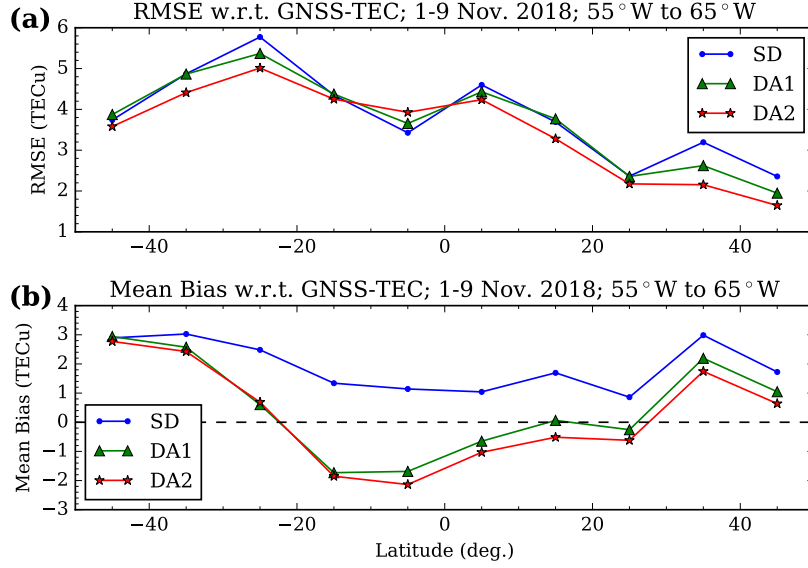
(a)

(b)

Figure 8. Latitudinal variability of RMSE (a) and mean bias (b) for SD (blue), DA1 (green), and DA2 (red) with respect to GNSS-TEC during 1-9 Nov. 2018 are shown. Clearly, for the DA2 the RMSE is smaller compared to other two cases and bias is closer to zero.

2. The GOLD T_{disk} and O/N_2 compare better with the WACCMX+DART analysis effective temperature and O/N_2 when compared with equivalent parameters from SD-WACCMX.

3. The RMSE (w.r.t. GOLD) improvements in the analyses effective temperature and O/N_2, when compared to their SD-WACCMX equivalents, are about 10.8% and 22.6%, respectively.

4. The RMSE between GNSS-TEC and analysis electron column density (ECD) is improved compared to that between GNSS-TEC and SD-WACCMX ECD. The improvement is about 10% for the assimilation that updates the O, O^+, and O_2 densities in addition to temperature.

These results indicate that the GOLD observations of the thermospheric temperature have a great potential to improve the operational and short term forecast of the thermosphere-ionosphere system.

Acknowledgments

References

Aa, E., Liu, S., Huang, W., Shi, L., Gong, J., Chen, Y., . . . Li, J. (2016, June). Regional 3-d ionospheric electron density specification on the basis of data assimilation of ground-based GNSS and radio occultation data. *Space Weather*, *14*(6), 433–448. doi: 10.1002/2016sw001363

Aksnes, A., Eastes, R., Budzien, S., & Dymond, K. (2006). Neutral temperatures in the lower thermosphere from N_2 Lyman-Birge-Hopfield (LBH) band profiles. *Geophysical Research Letters*, *33*(15). doi: 10.1029/2006gl026255

Anderson, J., Hoar, T., Raeder, K., Liu, H., Collins, N., Torn, R., & Avellano, A. (2009, September). The data assimilation research testbed: A community facility. *Bulletin of the American Meteorological Society*, *90*(9), 1283–1296. doi: 10.1175/2009bams2618.1

Anderson, J. L. (2001, December). An ensemble adjustment kalman filter for data assimilation. *Monthly Weather Review*, *129*(12), 2884–2903. doi: 10.1175/1520-0493(2001)129⟨2884:aeakff⟩2.0.co;2

Bust, G. S., Garner, T. W., & Gaussiran II, T. L. (2004). Ionospheric data assimilation three-dimensional (IDA3D): A global, multisensor, electron density specification algorithm. *Journal of Geophysical Research: Space Physics*,

109(A11). doi: 10.1029/2003ja010234

Bust, G. S., & Immel, T. J. (2020, March). IDA4D: Ionospheric data assimilation for the ICON mission. *Space Science Reviews*, *216*(3). doi: 10.1007/s11214-020-00648-z

Cantrall, C. E., Matsuo, T., & Solomon, S. C. (2019, October). Upper atmosphere radiance data assimilation: A feasibility study for GOLD far ultraviolet observations. *Journal of Geophysical Research: Space Physics*, *124*(10), 8154–8164. doi: 10.1029/2019ja026910

Chen, C. H., Lin, C. H., Matsuo, T., Chen, W. H., Lee, I. T., Liu, J. Y., . . . Hsu, C. T. (2016, June). Ionospheric data assimilation with thermosphere-ionosphere-electrodynamics general circulation model and GPS-TEC during geomagnetic storm conditions. *Journal of Geophysical Research: Space Physics*, *121*(6), 5708–5722. doi: 10.1002/2015ja021787

Codrescu, M. V., Fuller-Rowell, T. J., & Minter, C. F. (2004, November). An ensemble-type kalman filter for neutral thermospheric composition during geomagnetic storms. *Space Weather*, *2*(11). doi: 10.1029/2004sw000088

Codrescu, S. M., Codrescu, M. V., & Fedrizzi, M. (2018, January). An ensemble kalman filter for the thermosphere-ionosphere. *Space Weather*, *16*(1), 57–68. doi: 10.1002/2017sw001752

Correira, J., Evans, J. S., Lumpe, J. D., Krywonos, A., Daniell, R., Veibell, V., . . . Eastes, R. W. (2021, December). Thermospheric composition and solar EUV flux from the global-scale observations of the limb and disk (GOLD) mission. *Journal of Geophysical Research: Space Physics*, *126*(12). doi: 10.1029/2021ja029517

Datta-Barua, S., Bust, G. S., & Crowley, G. (2013, November). First storm-time plasma velocity estimates from high-resolution ionospheric data assimilation. *Journal of Geophysical Research: Space Physics*, *118*(11), 7458–7471. doi: 10.1002/2013ja019153

Eastes, R. W., McClintock, W. E., Burns, A. G., Anderson, D. N., Andersson, L., Aryal, S., . . . Woods, T. N. (2020, June). Initial observations by the GOLD mission. *Journal of Geophysical Research: Space Physics*, *125*(7). doi: 10.1029/2020ja027823

Eastes, R. W., Solomon, S. C., Daniell, R. E., Anderson, D. N., Burns, A. G., Eng-

land, S. L., ... McClintock, W. E. (2019, August). Global-scale observations of the equatorial ionization anomaly. *Geophysical Research Letters*, *46*(16), 9318–9326. doi: 10.1029/2019gl084199

Forsythe, V. V., Azeem, I., Blay, R., Crowley, G., Makarevich, R. A., & Wu, W. (2021, April). Data assimilation retrieval of electron density profiles from ionosonde virtual height data. *Radio Science*, *56*(5). doi: 10.1029/2021rs007264

Gelaro, R., McCarty, W., Suárez, M. J., Todling, R., Molod, A., Takacs, L., ... Zhao, B. (2017, July). The modern-era retrospective analysis for research and applications, version 2 (MERRA-2). *Journal of Climate*, *30*(14), 5419–5454. doi: 10.1175/jcli-d-16-0758.1

He, J., Yue, X., Le, H., Ren, Z., & Wan, W. (2020, March). Evaluation on the quasi-realistic ionospheric prediction using an ensemble kalman filter data assimilation algorithm. *Space Weather*, *18*(3). doi: 10.1029/2019sw002410

Hersbach, H., Bell, B., Berrisford, P., Hirahara, S., Horányi, A., Muñoz-Sabater, J., ... Thépaut, J.-N. (2020, June). The ERA5 global reanalysis. *Quarterly Journal of the Royal Meteorological Society*, *146*(730), 1999–2049. doi: 10.1002/qj.3803

Kodikara, T., Zhang, K., Pedatella, N. M., & Borries, C. (2021, May). The impact of solar activity on forecasting the upper atmosphere via assimilation of electron density data. *Space Weather*, *19*(5). doi: 10.1029/2020sw002660

Krywonos, A., Murray, D. J., Eastes, R. W., Aksnes, A., Budzien, S. A., & Daniell, R. E. (2012, September). Remote sensing of neutral temperatures in the Earth's thermosphere using the Lyman-Birge-Hopfield bands of N_2: Comparisons with satellite drag data. *Journal of Geophysical Research: Space Physics*, *117*(A9). doi: 10.1029/2011ja017226

Laskar, F. I., Eastes, R. W., Codrescu, M. V., Evans, J. S., Burns, A. G., Wang, W., ... Cai, X. (2021, August). Response of GOLD retrieved thermospheric temperatures to geomagnetic activities of varying magnitudes. *Geophysical Research Letters*, *48*(15). doi: 10.1029/2021gl093905

Laskar, F. I., Eastes, R. W., Martinis, C. R., Daniell, R. E., Pedatella, N. M., Burns, A. G., ... Codrescu, M. V. (2020, July). Early morning equatorial ionization anomaly from GOLD observations. *Journal of Geophysical Research: Space*

Physics, *125*(7). doi: 10.1029/2019ja027487

Laskar, F. I., McCormack, J. P., Chau, J. L., Pallamraju, D., Hoffmann, P., & Singh, R. P. (2019, August). Interhemispheric meridional circulation during sudden stratospheric warming. *Journal of Geophysical Research: Space Physics*, *124*(8), 7112–7122. doi: 10.1029/2018ja026424

Laskar, F. I., Pedatella, N. M., Codrescu, M. V., Eastes, R. W., Evans, J. S., Burns, A. G., & McClintock, W. (2021, January). Impact of GOLD retrieved thermospheric temperatures on a whole atmosphere data assimilation model. *Journal of Geophysical Research: Space Physics*, *126*(1). doi: 10.1029/2020ja028646

Lee, I. T., Matsuo, T., Richmond, A. D., Liu, J. Y., Wang, W., Lin, C. H., ... Chen, M. Q. (2012). Assimilation of formosat-3/cosmic electron density profiles into a coupled thermosphere/ionosphere model using ensemble kalman filtering. *Journal of Geophysical Research: Space Physics*, *117*(A10). doi: https://doi.org/10.1029/2012JA017700

Lin, C. Y., Matsuo, T., Liu, J. Y., Lin, C. H., Tsai, H. F., & Araujo-Pradere, E. A. (2015, January). Ionospheric assimilation of radio occultation and ground-based GPS data using non-stationary background model error covariance. *Atmospheric Measurement Techniques*, *8*(1), 171–182. doi: 10.5194/amt-8-171-2015

Liu, H.-L., Bardeen, C. G., Foster, B. T., Lauritzen, P., Liu, J., Lu, G., ... Wang, W. (2018, February). Development and validation of the whole atmosphere community climate model with thermosphere and ionosphere extension (WACCM-x 2.0). *Journal of Advances in Modeling Earth Systems*, *10*(2), 381–402. doi: 10.1002/2017ms001232

Marsh, D. R. (2011). Chemical–dynamical coupling in the mesosphere and lower thermosphere. In *Aeronomy of the earth's atmosphere and ionosphere* (pp. 3–17). Springer Netherlands. doi: 10.1007/978-94-007-0326-1_1

Matsuo, T., Lee, I.-T., & Anderson, J. L. (2013, March). Thermospheric mass density specification using an ensemble kalman filter. *Journal of Geophysical Research: Space Physics*, *118*(3), 1339–1350. doi: 10.1002/jgra.50162

McClintock, W. E., Eastes, R. W., Beland, S., Bryant, K. B., Burns, A. G., Correira, J., ... Veibel, V. (2020, May). Global-scale observations of the limb and disk mission implementation: 2. observations, data pipeline, and level 1

data products. *Journal of Geophysical Research: Space Physics*, *125*(5). doi: 10.1029/2020ja027809

McCormack, J. P., Harvey, V. L., Pedatella, N., Koshin, D., Sato, K., Coy, L., . . . Holt, L. A. (2021). Intercomparison of middle atmospheric meteorological analyses for the northern hemisphere winter 2009-2010. *Atmospheric Chemistry and Physics Discussions*, *2021*, 1–48. doi: 10.5194/acp-2021-224

McCormack, J. P., Hoppel, K., Kuhl, D., de Wit, R., Stober, G., Espy, P., . . . Hibbins, R. (2017, February). Comparison of mesospheric winds from a high-altitude meteorological analysis system and meteor radar observations during the boreal winters of 2009–2010 and 2012–2013. *Journal of Atmospheric and Solar-Terrestrial Physics*, *154*, 132–166. doi: 10.1016/j.jastp.2016.12.007

Mehta, P. M., Linares, R., & Sutton, E. K. (2018, May). A quasi-physical dynamic reduced order model for thermospheric mass density via hermitian space-dynamic mode decomposition. *Space Weather*, *16*(5), 569–588. doi: 10.1029/2018sw001840

Pedatella, N. M., Anderson, J. L., Chen, C. H., Raeder, K., Liu, J., Liu, H.-L., & Lin, C. H. (2020, September). Assimilation of ionosphere observations in the whole atmosphere community climate model with thermosphere-ionosphere EXtension (WACCMX). *Journal of Geophysical Research: Space Physics*, *125*(9). doi: 10.1029/2020ja028251

Pedatella, N. M., Liu, H.-L., Marsh, D. R., Raeder, K., Anderson, J. L., Chau, J. L., . . . Siddiqui, T. A. (2018, April). Analysis and hindcast experiments of the 2009 sudden stratospheric warming in WACCMX+DART. *Journal of Geophysical Research: Space Physics*, *123*(4), 3131–3153. doi: 10.1002/2017ja025107

Pedatella, N. M., Raeder, K., Anderson, J. L., & Liu, H.-L. (2014, August). Ensemble data assimilation in the whole atmosphere community climate model. *Journal of Geophysical Research: Atmospheres*, *119*(16), 9793–9809. doi: 10.1002/2014jd021776

Remsberg, E. E., Marshall, B. T., Garcia-Comas, M., Krueger, D., Lingenfelser, G. S., Martin-Torres, J., . . . Thompson, R. E. (2008, September). Assessment of the quality of the version 1.07 temperature-versus-pressure profiles of the middle atmosphere from TIMED/SABER. *Journal of Geophysical Research*, *113*(D17). doi: 10.1029/2008jd010013

Ren, D., & Lei, J. (2020, August). Evaluation of physics-based data assimilation system driven by neutral density data from a single satellite. *Space Weather*, *18*(8). doi: 10.1029/2020sw002504

Rideout, W., & Coster, A. (2006, May). Automated GPS processing for global total electron content data. *GPS Solutions*, *10*(3), 219–228. doi: 10.1007/s10291-006 -0029-5

Rienecker, M. M., Suarez, M. J., Gelaro, R., Todling, R., Bacmeister, J., Liu, E., . . . Woollen, J. (2011, July). MERRA: NASA's modern-era retrospective analysis for research and applications. *Journal of Climate*, *24*(14), 3624–3648. doi: 10.1175/jcli-d-11-00015.1

Schwartz, M. J., Lambert, A., Manney, G. L., Read, W. G., Livesey, N. J., Froide-vaux, L., . . . Wu, D. L. (2008, May). Validation of the aura microwave limb sounder temperature and geopotential height measurements. *Journal of Geophysical Research*, *113*(D15). doi: 10.1029/2007jd008783

Song, R., Hattori, K., Zhang, X., & Yoshino, C. (2021, August). The three-dimensional ionospheric electron density imaging in japan using the approximate kalman filter algorithm. *Journal of Atmospheric and Solar-Terrestrial Physics*, *219*, 105628. doi: 10.1016/j.jastp.2021.105628

Strickland, D. J., Evans, J. S., & Paxton, L. J. (1995). Satellite remote sensing of thermospheric o/n2and solar EUV: 1. theory. *Journal of Geophysical Research*, *100*(A7), 12217. Retrieved from https://doi.org/10.1029/95ja00574 doi: 10.1029/95ja00574

Sutton, E. K. (2018, June). A new method of physics-based data assimilation for the quiet and disturbed thermosphere. *Space Weather*, *16*(6), 736–753. doi: 10 .1002/2017sw001785

Vierinen, J., Coster, A. J., Rideout, W. C., Erickson, P. J., & Norberg, J. (2016, March). Statistical framework for estimating GNSS bias. *Atmospheric Measurement Techniques*, *9*(3), 1303–1312. doi: 10.5194/amt-9-1303-2016

Wang, H., Fuller-Rowell, T. J., Akmaev, R. A., Hu, M., Kleist, D. T., & Iredell, M. D. (2011, December). First simulations with a whole atmosphere data assimilation and forecast system: The january 2009 major sudden stratospheric warming. *Journal of Geophysical Research: Space Physics*, *116*(A12). doi: 10.1029/2011ja017081